Nano Research

Open Access

Research Article

Enhanced N_2 electroreduction activity of single-atom catalysts: Modulating the linear scaling relationship by coordination engineering and dual-site strategies

Renyi Li[1], Caimu Wang[1], Jiao Zhang[1], and Wei Guo[1,2] ✉

[1] *Centre for Quantum Physics, Key Laboratory of Advanced Optoelectronic Quantum Architecture and Measurement (MOE), School of Physics, Beijing Institute of Technology, Beijing 100081, China*
[2] *Frontiers Science Center for High Energy Material (MOE), Beijing Institute of Technology, Beijing 100081, China*

Cite this article: *Nano Research*, **2025**, *18*, 94907212. https://doi.org/10.26599/NR.2025.94907212

ABSTRACT: The volcano plot is widely used to elucidate the activity trends among different catalysts, thereby effectively screening and guiding catalyst design. However, the inherent linear scaling relationship (LSR) constrains the breakthrough in the activity of catalysts, and the understanding of the activity limit in volcano plot is still ambiguous. In this work, by employing first-principles calculations and microkinetic modeling, we proposed coordination engineering (CE) and dual-site (DS) strategies to surpass the Sabatier's limitation of WS_2-supported TM (TM@WS_2) single-atom catalysts (SACs) for electrocatalytic nitrogen reduction reaction (eNRR). We found that the LSR between $\Delta G(*N_2 \rightarrow *N_2H)$ and $\Delta G(*NH_2 \rightarrow *NH_3)$ was optimized to be closer to the ideal space of eNRR activity after modulating TM@WS_2 SACs by these two design strategies. By combining the reaction selectivity trend plot, we picked out N-Os@WS_2, C-Ir@WS_2, Fe_2@WS_2, and Ru_2@WS_2 as optimal eNRR catalysts with low limiting potential (U_L), and N-Os@WS_2 SAC (U_L: –0.28 V) outperforms the best eNRR catalyst among TM@WS_2 SACs. By constructing explicit solvent models, we conducted a detailed study on the reaction kinetics of proton transfer over these four catalysts. We propose that the activity enhancement in TM@WS_2 SACs for eNRR can be attributed to the ligand effect and geometric effect brought about by CE and DS strategies, improving the donation-backdonation process of electron transfer between N_2 and the active sites. The designed catalyst has certain resistance to demetallization and agglomeration under simulated solvent environment. This work provides a feasible design strategy for the activity enhancement of SACs and brings a new perspective to deeply understanding the volcano plot in heterogeneous catalysis.

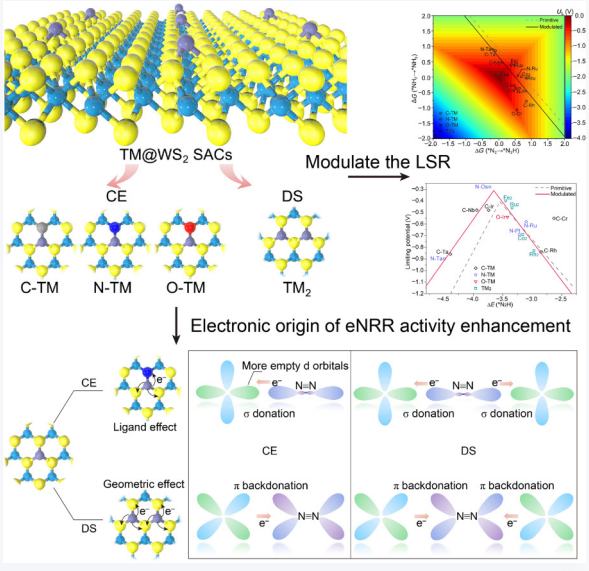

KEYWORDS: linear scaling relationship, volcano plot, single-atom catalysts, density functional theory (DFT), electrochemical nitrogen reduction

1 Introduction

Volcano plots are widely employed to describe the activity trend of heterogeneous catalytic reactions and intuitively illustrate the region with the highest catalytic activity. Understanding adsorption trends of intermediates, reaction activity/selectivity trends, electronic structure origins, and reaction mechanisms through theoretical calculations can provide deeper insights into catalytic volcano plots, aiding in the design and synthesis of efficient heterogeneous catalysts [1–4]. A volcano curve constructed from a single descriptor or a three-dimensional (3D) volcano plot established from pairs of descriptors can accurately reflect the activity trend and provide a basis for effective screening, prediction, and rational design of catalysts [5]. The inherent Sabatier's limitation makes it

Received: October 27, 2024; **Revised:** December 19, 2024
Accepted: December 23, 2024

✉Address correspondence to weiguo7@bit.edu.cn

difficult to break through the catalytic activity, which stems from the linear scaling relationship (LSR) between the adsorption energies of similar reaction intermediates on different catalyst surfaces [6, 7]. The LSR is related to the electronic structure of the catalyst surface [8]. LSRs between the adsorption energies of different intermediates lead to a delicate balance in the interaction between the key intermediate and the catalyst surface near the optimal activity region in a volcano plot (neither too strong nor too weak interaction), which enables the adsorption and activation of reactants or intermediates on the catalyst surface, and is beneficial for the desorption of products as well. For examples, by constructing catalytic atom pairs on porous carbon, a balance between CO_2 adsorption and CO desorption can be achieved, thereby surpassing the electrocatalytic activity of single-atom catalysts (SACs) for CO_2 reduction [9]. By manipulating the intermetallic distance and charge distribution of bimetallic pair sites, bridge-like adsorption configuration of OOH can be achieved, thereby enhancing the cleavage of the O–O bond and circumventing the Sabatier's constraints imposed by the LSR during the oxygen reduction reaction (ORR) [10].

In the electrocatalytic nitrogen reduction reaction (eNRR), the adsorption energy of *N (ΔE(*N)) serves as a good descriptor of reaction activity. In this context, Mo, Fe, Rh, and Ru have been predicted as optimal active surfaces, with corresponding ΔE(*N) values of approximately 0 to −1 eV [11]. When the adsorption of *N is weak, N_2 adsorption and the first proton transfer step ($N_2(g) + H^+ + e^- \rightarrow {}^*N_2H$) on transition metal (TM) surfaces determine the onset potential of the associative mechanism. When the adsorption of *N is too strong, the ${}^*NH_2 + H^+ + e^- \rightarrow NH_3(g)$ step limits the onset potential of the stepped TM surfaces. Therefore, the optimal eNRR catalyst requires a trade-off between improving the stability of $*N_2H$ and decreasing the stability of $*NH_2$ [12–16]. In the 3D volcano plot of eNRR constructed using descriptors of the free energy of *NNH (ΔG(*NNH)) and the free energy of $*NH_2$ (ΔG(*NH_2)), the LSR between ΔG(*NNH) and ΔG(*NH_2) constrains the approach of TM surfaces towards the ideal active region [17]. TM SACs can access an activity space beyond the reach of TM surfaces by breaking the LSR between ΔG(*NNH) and ΔG(*NH_2) on TM surfaces. Previous studies have shown that the LSR of TM SACs supported on g-C_3N_4 and N-doped carbon is more advantageous than that of TM surfaces [1, 17, 18]. Currently, many types of substrates supported SACs have been reported (polymeric carbon nitride, TM borides, black phosphorus, nitrogenated carbon nanotubes, TiO_2, MoS_2, and PtS_2), and their eNRR activity can be described by the adsorption energy of key intermediates [19–25]. Indeed, due to the presence of LSR between ΔG(*NNH) and ΔG(*NH_2) on TM SACs, there is still significant room for improvement in eNRR activity. eNRR activity can be enhanced through modulation of the adsorption energies of key intermediates and LSRs on specific substrates-supported TM SACs, but the fundamental mechanisms remain elusive. Differences in electronic structure between TM SACs supported on different substrate materials (different coordination structures) result in different slopes and intercepts for the LSR between ΔG(*NNH) and ΔG(*NH_2), exhibiting diverse eNRR activity trends [1]. In our previous work, we introduced TM single atoms (SAs) onto the surface of monolayer WS_2 (TM@WS_2) to create atomic protrusion sites that induce interfacial polarization, facilitating the activation and reduction of N_2 [26]. Although the activity trends of eNRR are well characterized by volcano maps, further exploration of the active space of TM@WS_2 is warranted. However, the limitation on TM SACs is that it is difficult to optimize the adsorption strength of multiple reaction intermediates at the same time, and construction of catalytic architectures with dual-site (DS) has the potential to overcome this limitation [27, 28]. These works inspire us to consider coordination engineering (CE) of the active site and constructing TM DS as potential schemes to break through the constraints of LSRs or to seek more suitable LSRs.

In this study, taking our previously reported TM@WS_2 SACs as an example [26], we found that CE of single TM active site and construction of TM DS can optimize LSRs in eNRR and surpass the volcanic peak of TM@WS_2 SACs. As shown in Fig. 1(a), by introducing C, N, O and substituting one S atom into TM@WS_2 SACs, we controlled the local structure and coordination environment of the single TM active site, resulting in C, N, O-doped WS_2-supported TM (C, N, O-TM@WS_2) SACs. Dispersive TM DS catalysts (TM_2@WS_2) can be formed by constructing dual-adjacent single TM active site. Currently, Pt@WS_2 SACs have been synthesized by using the site-specific electrodeposition technique [29]. In experiments, C, N, and O doped WS_2 can be achieved by employing the hydrothermal method [30], one-step sol–gel method [31], and iron oxide-assisted atmospheric pressure chemical vapor deposition method [32]. Although experimental synthesis of TM_2@WS_2 has not been reported, the preparation of TM DS on carbon-based supports, CeO_2, and TiO_2 is well-documented [33–35]. Therefore, the CE and DS strategies proposed in this work are feasible. According to the different structures of dual-metal sites, the dual-metal sites in dual-atom catalysts (DACs) can be classified into two separated heterometallic sites, two linked homometallic sites, and two linked heterometallic sites [27]. The structures of DACs with two linked homometallic sites are similar to the structures of TM dual-site (TM_2) in our work, where two metal sites can synergistically adsorb and activate N_2. Typically, pairs of homonuclear or heteronuclear metal atoms are anchored to the N-doped carbon substrate to form stable DACs [36, 37]. In our work, homonuclear TM atom pairs are directly anchored to the surface of pristine WS_2 to form the adjacent dual-metal sites via S atoms coordination. In addition, Fe atom pairs (Fe_2) anchored on the surface of pristine MoS_2 can be synthesized experimentally [38]. In this work, TM_2@WS_2 is adopted as the abbreviation of the TM DS catalysts to distinguish the corresponding SACs (TM@WS_2 and C/N/O-TM@WS_2). Based on a series of screening strategies and established eNRR volcano plots, we predict that N-Os@WS_2, C-Ir@WS_2, Fe_2@WS_2, and Ru_2@WS_2 exhibit high eNRR activity and selectivity. Specifically, N-Os@WS_2 surpasses the Sabatier's limitation of TM@WS_2 SACs. Additionally, employing explicit solvent models, we further investigated eNRR kinetics of N-Os@WS_2, C-Ir@WS_2, Fe_2@WS_2, and Ru_2@WS_2. We elucidated the fundamental reasons for the enhanced eNRR activity resulting from the CE and DS strategies at the electronic level. The designed catalyst showed excellent stability in aqueous solution environment.

2 Computational methods

Spin-polarized density functional theory (DFT) calculations were performed by Vienna *ab initio* simulation program (VASP) [39, 40]. The electronic structures were calculated by using device studio-projector augmented wave (DS-PAW) package (a module integrated in Device Studio) [41]. The ion-electron interaction and electronic exchange-correlation energy were described by projector augmented wave (PAW) [42] and Perdew–Burke–Ernzerhof (PBE) generalized gradient approximation (GGA) [43]. The plane-wave

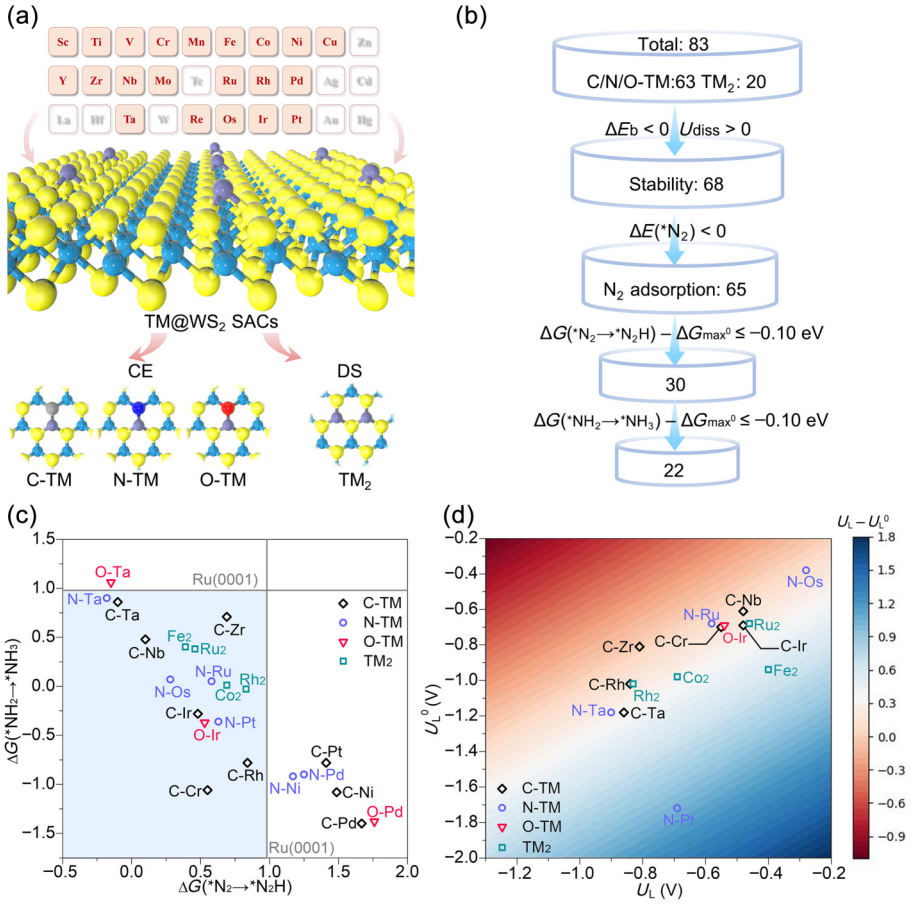

Figure 1 Design and screening of catalysts. (a) Modulation of TM@WS_2 SACs via CE and DS strategies. C-TM, N-TM, O-TM, and TM_2 represent TM SA coordinated with C, N and O, and TM DS on WS_2 (C-TM@WS_2, N-TM@WS_2, O-TM@WS_2, and TM_2@WS_2). (b) Screening of potential eNRR catalysts with enhanced activity compared to TM@WS_2 SACs. ΔG_{max}^0 represents the maximum free energy change for eNRR on TM@WS_2 SACs. ΔE_b and U_{diss} represent binding energy and dissolution potential of anchored TM atoms. A negative value of the binding energy and a positive value of the dissolution potential mean that the TM atom is thermodynamically and electrochemically stable on WS_2 according to the formulas in the ESM. $\Delta G(*N_2 \rightarrow *N_2H)$ and $\Delta G(*NH_2 \rightarrow *NH_3)$ are the free energy changes of the first and last protonation steps, respectively. (c) Screening of potential eNRR catalysts with higher activity than Ru(0001) surface. (d) The contour plot of the U_L of designed catalysts versus the U_L^0 of TM@WS_2 SACs. U_L represents the limiting potential for eNRR of C-TM@WS_2, N-TM@WS_2, O-TM@WS_2, and TM_2@WS_2. U_L^0 denotes the limiting potential for eNRR of TM@WS_2 SACs. The value of the limiting potential (see NOTE in the ESM) can characterize the activity of eNRR. The more positive the value of limiting potential, the higher the eNRR activity. Color labels: S (yellow), W (cyan), C (grey), N (blue), O (red), and anchored TM atom (lavender).

energy cutoff was set to 450 eV. Atomic force convergence criterion was set to 0.02 eV·Å^{-1}. The convergence criterion of the electronic self-consistent iteration was set to 10^{-5} eV. The vacuum region was set to 15 Å to avoid the interaction caused by periodic images. We selected the 4 × 4 × 1 supercell of WS_2 as the support. The surface Monkhorst-Pack meshes of 3 × 3 × 1 k-point grid was used for structural optimization [44]. The van der Waals correction was considered by using Grimme's DFT-D3 method with Becke-Johnson damping function [45]. Previous studies have shown that the impact of solvent effects on the free energy of eNRR could be much smaller than the energy differences between different materials [46–48]. Taking Os@WS_2 and N-Os@WS_2 as examples, we tested the free energy diagrams of eNRR under vacuum conditions and under implicit solvent conditions (Fig. S1 in the Electronic Supplementary Material (ESM)) [49]. The results indicated that the potential-determining step (PDS) of eNRR remains unchanged under both conditions with and without implicit solvent, and the corresponding free energy change (ΔG_{PDS}) had an error of only 0.09 to 0.11 eV, which is consistent with most published theoretical studies [46, 50]. The use of the PBE functional can reproduce many experimental results well without considering solvation effects [51, 52]. Therefore, the slight influence of solvent effect on the activity trend was acceptable. The detailed methods of free energy calculations and microkinetic simulation were given in the ESM.

3 Results and discussion

3.1 Design and screening of catalysts

Due to the toxicity of Cd and Hg, as well as the radioactivity of Tc and lanthanide elements, these elements are not considered (Fig. 1(a)). Our previous work [26] has shown that single Ag and Au atoms have poor thermodynamic stability when adsorbed on the basal plane of WS_2. Additionally, anchoring single Hf and W atoms on the WS_2 surface causes structural deformation, and single Zn atom only physically adsorbs on the surface of WS_2. Therefore, Ag, Au, Hf, W, and Zn are excluded. Based on these two strategies, we constructed 83 catalysts, as shown in Fig. 1(b), with 63 catalysts generated from the CE strategy and 20 catalysts obtained from the DS strategy. The atomic structure of Mo_2@WS_2 is found to be unstable after relaxation and thus has been excluded (Fig. S2 in the

ESM). To ensure the stability of the designed catalysts under both thermodynamic and electrochemical conditions, the binding energy (ΔE_b) and dissolution potential (U_{diss}) of anchored TM atoms were calculated (see NOTE in the ESM), with 68 catalysts meeting the screening criteria of structural stability (Figs. S3 and S4 in the ESM). The adsorption of N_2 on these stable catalysts is an exothermic process, i.e., the adsorption energy of N_2 is less than zero (Figs. S5 and S6 in the ESM). As shown in Fig. S6(d) in the ESM, due to structural deformation or migration of TM atoms upon N_2 adsorption, $Pd_2@WS_2$, $Ta_2@WS_2$, and $Pt_2@WS_2$ are excluded. In most cases, the first protonation step ($*N_2 + H^+ + e^- \rightarrow *N_2H$) or the last protonation step ($*NH_2 + H^+ + e^- \rightarrow *NH_3$) is considered as the PDS for eNRR [23]. By calculating the ΔG for these two steps, promising catalysts can be rapidly and effectively picked out. To ensure the availability of catalysts with enhanced eNRR activity, $\Delta G(*N_2 \rightarrow *N_2H)$ and $\Delta G(*NH_2 \rightarrow *NH_3)$ need to be decreased by at least 0.1 eV compared to $\Delta G_{max}{}^0$ (ΔG of PDS) of $TM@WS_2$ SACs (Figs. S7 and S8 in the ESM). As shown in Fig. S8(c) in the ESM, the adsorption of NH_3 on $Cu_2@WS_2$ results in an unstable Cu atom on WS_2 basal plane, and thus $Cu_2@WS_2$ is also excluded. Ultimately, with this customized screening strategy, we were able to pick out 22 catalysts with improved eNRR activity from the 83 candidate catalysts.

To further screen, the activity of the selected catalysts was compared with benchmark Ru(0001) surface [1, 50]. As shown in Fig. 1(c), there still exists a LSR between the $\Delta G(*N_2 \rightarrow *N_2H)$ and $\Delta G(*NH_2 \rightarrow *NH_3)$ for different catalysts. Due to the LSRs between the adsorption strength of intermediates, the lower the ΔG for the first protonation step, the more challenging it will be for the last protonation step to occur. The blue region represents where both $\Delta G(*N_2 \rightarrow *N_2H)$ and $\Delta G(*NH_2 \rightarrow *NH_3)$ are smaller than the ΔG_{max} of Ru(0001) (~ 0.98 eV), enabling us to identify 15 potential catalysts with high eNRR activity. For these 15 catalysts, we calculated the free energy diagram of eNRR under the distal, alternative, enzymatic and consecutive mechanisms, and obtained the limiting potential (U_L) under the optimal reaction pathway (Figs. S9–S13 in the ESM). As shown in Fig. 1(d), we can construct contour plots of eNRR activity with U_L and $U_L{}^0$. U_L is the limiting potential for eNRR of modulated catalysts, and the formula is shown in the ESM. $U_L{}^0$ is the limiting potential for eNRR of $TM@WS_2$ SACs. The red space indicates a decrease in the eNRR activity of the designed catalysts, and the blue area indicates an increase in the catalytic activity. Most of the designed catalysts are distributed in the white region between the blue and red regions, where U_L is elevated by 0.10 to 0.60 V compared to $U_L{}^0$. N-$Pt@WS_2$ SAC is in the blue region, and its eNRR activity (–0.69 V) is significantly increased by 1.03 V compared with $Pt@WS_2$ SAC (–1.72 V). In the section of electronic structure analysis, we will explain the reason for the enhanced eNRR activity of N-$Pt@WS_2$ SAC. The U_L (–0.81 V) of C-$Zr@WS_2$ SAC is equal to the $U_L{}^0$ of $Zr@WS_2$ SAC. The calculated reaction free energies show that the optimal eNRR pathway on C-$Zr@WS_2$ SAC follows the distal mechanism, with PDS of $*NNH_2$ reduction to *N, rather than the first or last protonation step (Fig. S9 in the ESM). Therefore, C-$Zr@WS_2$ SAC is excluded because it does not meet the demand for the enhancement of eNRR activity. Finally, 14 designed catalysts were identified to have higher eNRR activity than $TM@WS_2$ SACs, and their activity was higher than that of Ru(0001) surface.

Figure 2 shows the free energy diagrams of N-$Os@WS_2$, C-$Ir@WS_2$, $Fe_2@WS_2$, and $Ru_2@WS_2$ along the most favorable eNRR route and the optimized structures of different reaction intermediates. The two adsorption configurations of N_2 on these four catalysts lead to two different reaction pathways. The end-on adsorption of N_2 on N-$Os@WS_2$ and C-$Ir@WS_2$ SACs triggers the distal reaction pathway, while the side-on adsorption on $Fe_2@WS_2$ and $Ru_2@WS_2$ opens the enzymatic reaction pathway. As shown in Figs. 2(a) and 2(b), the distal N atom undergoes three protonation steps to form the first NH_3, and the remaining surface N species are protonated three times to produce the second NH_3. The PDS of N-$Os@WS_2$ and C-$Ir@WS_2$ SACs are the protonation of $*N_2$ to *NNH. After applying an electrode potential of –0.28 and –0.48 V, respectively, ΔG_{max} is decreased to 0, and the remaining electrochemical reaction steps are thermodynamically spontaneous. As shown in Figs. 2(c) and 2(d), the two N atoms of N_2 bind to the two TM active sites respectively and are subsequently attacked four times alternately by proton-electron pairs to form $*NH_2*NH_2$ intermediates. After the fifth protonation reaction, the N≡N bond dissociates, resulting in the formation and desorption of an NH_3. The remaining NH_2 tends to adsorb between the two TM sites. The second NH_3, formed by protonation of $*NH_2$, prefers to be adsorbed at a single TM site. The PDS of $Fe_2@WS_2$ and $Ru_2@WS_2$ are the last protonation step and the first protonation step, respectively, and the corresponding U_L are –0.40 and –0.46 V, respectively. These four catalysts exhibit outstanding eNRR activity, with U_L less than half that of Ru(0001) surface [50].

3.2 Linear scaling relationships and activity trends

Correlating the U_L of screened catalysts with one or two descriptors is an effective means to directly reflect the activity trend of eNRR. By comparing the activity trend of the modulated $TM@WS_2$ SACs (C-$TM@WS_2$, N-$TM@WS_2$, O-$TM@WS_2$, and $TM_2@WS_2$) and $TM@WS_2$ SACs, it is conducive to understand the difference of activity among different catalysts and the reasons for the enhancement of activity. As shown in Figs. 3(a) and 3(b), the adsorption strength of $*N_2H$ and $*NH_2$ is correlated with the protonation process of $*N_2$ and $*NH_2$, respectively, but these two LSRs show opposite trends, which has also been reflected in previous studies [24, 26]. Generally, for the first protonation process, the stable N≡N triple bond needs to be broken to form an unstable $*N_2H$ intermediate, and the process is thermodynamically unfavorable with a more positive $\Delta G(*N_2 \rightarrow *N_2H)$. Thus, when the $*N_2H$ intermediate is relatively stable, that is, the more negative $\Delta E(*N_2H)$ is, the lower $\Delta G(*N_2 \rightarrow *N_2H)$ is. The half-filled sp^3 hybrid orbital of NH_2 can be strongly coupled with the d orbital of the TM active site, resulting in a relatively stable $*NH_2$ adsorbed species. However, the sp^3 hybrid orbital of NH_3 is completely filled, making its adsorption on the TM atom weaker than $*NH_2$, which usually leads to an uphill $\Delta G(*NH_2 \rightarrow *NH_3)$. Therefore, weakening the adsorption strength of $*NH_2$, i.e., more positive $\Delta E(*NH_2)$, can mitigate the ascending $\Delta G(*NH_2 \rightarrow *NH_3)$. The modulated LSRs have similar slopes to the primitive LSRs, but the intercepts are different. It is worth noting that C-$Cr@WS_2$ SAC deviates from the LSR between $\Delta E(*N_2H)$ and $\Delta G(*N_2 \rightarrow *N_2H)$ (Fig. 3(a)), exhibiting a relatively lower $\Delta G(*N_2 \rightarrow *N_2H)$. The modulated LSR yields a lower $\Delta G(*NH_2 \rightarrow *NH_3)$ than the primitive LSR (Fig. 3(b)). In the protonation steps of eNRR, $\Delta G(*N_2 \rightarrow *N_2H)$ and $\Delta G(*NH_2 \rightarrow *NH_3)$ are usually selected to describe the activity trend due to the relatively high free energy, which have also been confirmed in previous studies [1, 53]. Based on the LSR analysis, we constructed a contour volcano map of U_L as a function of $\Delta G(*N_2 \rightarrow *N_2H)$ and

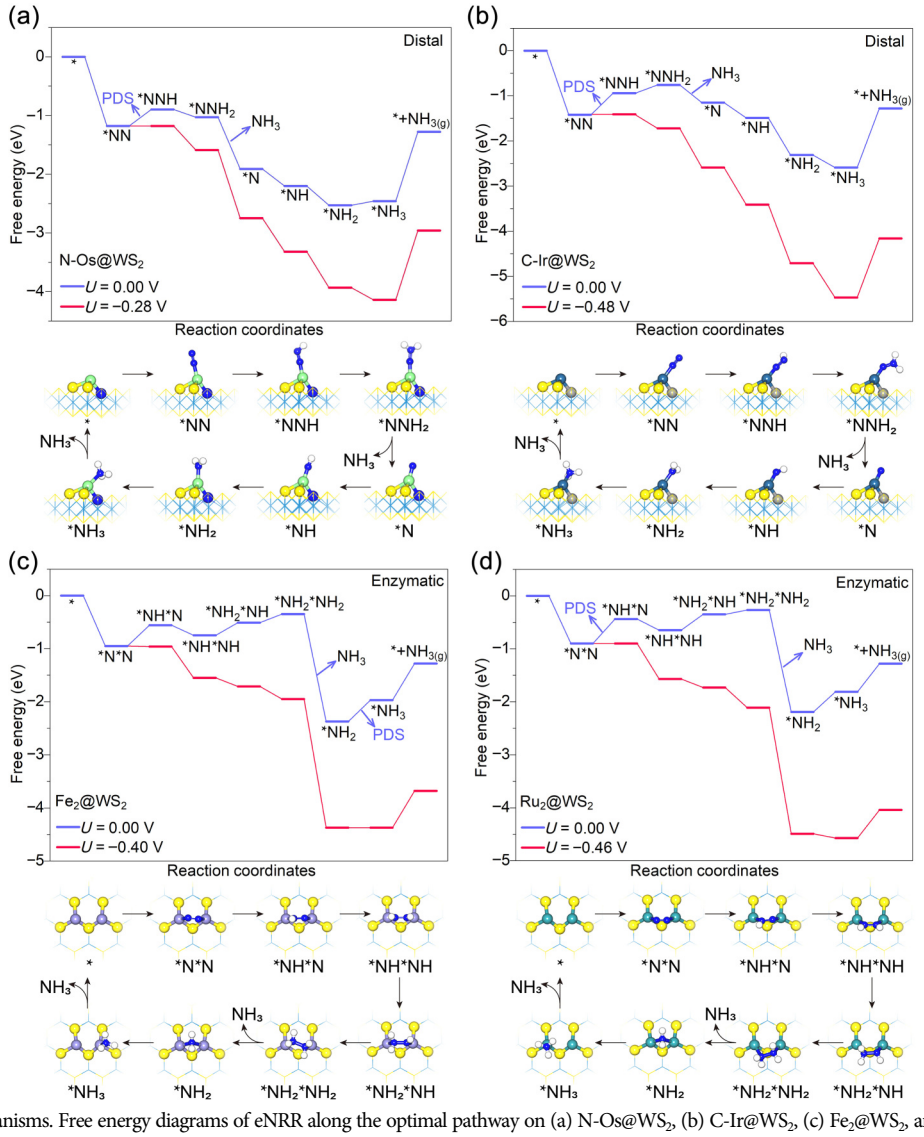

Figure 2 Reaction mechanisms. Free energy diagrams of eNRR along the optimal pathway on (a) N-Os@WS_2, (b) C-Ir@WS_2, (c) Fe_2@WS_2, and (d) Ru_2@WS_2. The line model represents the WS_2 substrate. Color labels: S (yellow), N (blue), C (black), H (white), Os (green), Ir (dark cyan), Fe (lavender), and Ru (cyan).

ΔG(*NH_2→*NH_3) in Fig. 3(c) to comprehensively understand the effects of CE and DS strategies on the activity trend of TM@WS_2 SACs. In Fig. 3(c), a prominent region of maximum eNRR activity (depicted in deep red triangles) catches the eye. If ΔG(*N_2→*N_2H) and ΔG(*NH_2→*NH_3) can be independently adjusted, it would be possible to achieve the access to the ideal activity region. However, the LSR of ΔG(*N_2→*N_2H) and ΔG(*NH_2→*NH_3) leads to the inherent limitation of catalytic activity, which is probably because both ΔE(*N_2H) and ΔE(*NH_2) scale linearly with the adsorption energies of other intermediates. Although there is still an LSR between ΔG(*N_2→*N_2H) and ΔG(*NH_2→*NH_3) for the modulated TM@WS_2 SACs, the modulated LSR is closer to the ideal space of eNRR activity than the primitive LSR. Most modulated TM@WS_2 SACs can enter the activity space that is inherently inaccessible to TM@WS_2 SACs. N-Os@WS_2 SAC is distributed at the edge of the ideal region and exhibits excellent eNRR activity. Our previous work suggests that Pt@WS_2 SAC was located in the green area [26], while the modulated Pt@WS_2 SAC (N-Pt@WS_2 SAC) via the CE strategy enters the red area, and its U_L is increased by 1.03 V. Compared to Cr@WS_2 SAC, the ΔG(*NH_2→*NH_3) of C-Cr@WS_2 SAC decreases from 0.14 to −1.06 eV, and the ΔG(*N_2→*N_2H) decreases from 0.70 to 0.55 eV, leading to the deviation of C-Cr@WS_2 SAC from the primitive LSR, with U_L elevated by 0.15 V. By discussing the LSRs between the adsorption energies of the key intermediates (*N_2H and *NH_2) and ΔG of the first/last protonation, we realize that the adsorption energy of *N_2H also seems to describe the activity trend of eNRR. As displayed in Fig. 3(d), the scatter data of U_L of different catalysts are obviously divided into two branches by ΔE(*N_2H), resulting in two LSRs with different slopes and intercepts, which converge to form a volcanic map structure. Compared to the primitive eNRR volcano plot, the highest point of the modulated volcano map is significantly higher, and the U_L (−0.28 V) of N-Os@WS_2 SAC is predicted to exceed the peak of the primitive volcano map. The relationship between ΔE(*N_2H) and U_L follows the Sabatier principle, and too strong or too weak *N_2H adsorption is not conducive to eNRR activity. For examples, the adsorption strength of *N_2H on N-Ta@WS_2 and C-Ta@WS_2 is stronger (−4.49 and −4.39 eV) and exhibits higher U_L (−0.90 and −0.86 V). Considering that the adsorption energy of the intermediates is linearly correlated, the binding strength of excessively strong *N_2H at N-Ta@WS_2 and C-Ta@WS_2 can weaken the ΔG of the first protonated step, but also lead to the

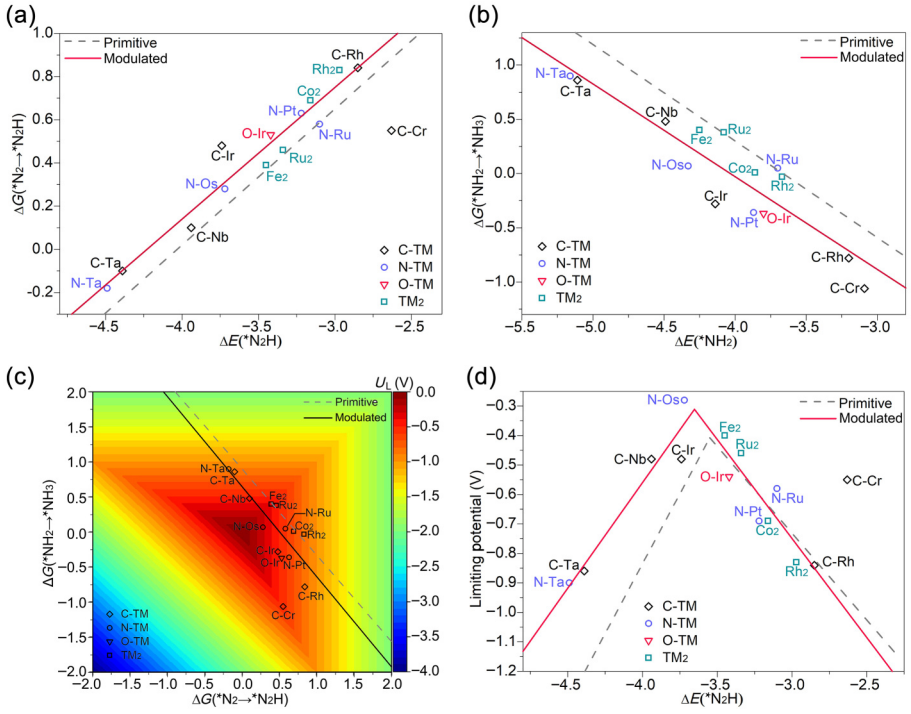

Figure 3 Activity trends of eNRR. The LSR between (a) $\Delta E(*N_2H)$ and $\Delta G(*N_2 \rightarrow *N_2H)$, (b) $\Delta E(*NH_2)$ and $\Delta G(*NH_2 \rightarrow *NH_3)$. (c) 3D volcano plot of eNRR, where the U_L of eNRR is described by $\Delta G(*N_2 \rightarrow *N_2H)$ and $\Delta G(*NH_2 \rightarrow *NH_3)$. (d) Single parameter volcano plot described by $\Delta E(*N_2H)$. The dashed and solid lines represent the LSRs described by $TM@WS_2$ SACs and modulated $TM@WS_2$ SACs (C-$TM@WS_2$, N-$TM@WS_2$, O-$TM@WS_2$, and $TM_2@WS_2$), respectively. The data for fitting the dashed lines are derived from our previously published work [26].

strengthening of similar $*NH_2$ reaction species, resulting in the formation and desorption of the product NH_3 as the PDS of eNRR. When the adsorption strength of $*N_2H$ at C-$Rh@WS_2$ becomes weak (–2.85 eV), the protonation of $*N_2$ to $*N_2H$ will become the PDS of eNRR (U_L: –0.84 V) due to the relatively high free energy level of $*N_2H$. The optimal $*N_2H$ adsorption energy window predicted by the modulated eNRR volcano map shifts about 0.10 eV in the direction of stronger adsorption. From the slope and intercept of the left and right branches of the volcano map, the modulated left branch is closer to the direction of U_L decrease (more positive value) than the primitive left branch. A previous study showed that the binding/antibonding orbital population of TM SACs and *N adatom was the origin of the observed adsorption trend of intermediates during eNRR, thus explaining the differences in LSRs between adsorbed intermediates in different coordination environments [1]. In addition, the eNRR activity trend of phosphorene anchored TM SACs can be described by the percentage of empty d orbital of metal sites [54]. In this work, the changes in LSRs caused by CE and DS strategies may be related to differences in the electronic structures of the different metal active centers, such as the d-orbital occupation of the metal site, which can improve the electron transfer between the active site and N_2, which will be detailed in the electronic structure analysis section.

3.3 Reaction selectivity

In acidic aqueous electrolytes, the competitive hydrogen evolution reaction (HER) of the cathode usually leads to the formation of H_2, which reduces the Faradic efficiency of eNRR. Figure 4(a) shows the competition between eNRR and HER on the active sites under acidic conditions. As shown in Fig. 4(b), the eNRR selectivity of catalysts can be evaluated by comparing the U_L of eNRR and HER. The top left and bottom right regions correspond to the areas where HER and eNRR are gradually enhanced, respectively. The HER activity is higher than the eNRR activity in C-Rh, C-Cr, N-$Ru@WS_2$ SACs, and $Co_2@WS_2$. Among them, the U_L for HER on C-$Rh@WS_2$ SAC is only –0.07 V, making it a potential HER catalyst. The U_L for HER and eNRR are comparable on C-Nb, N-$Ta@WS_2$ SACs, and $Rh_2@WS_2$, suggesting that these three catalysts can potentially produce both H_2 and NH_3. C-Ta, N-Pt, and O-$Ir@WS_2$ SACs exhibit moderate eNRR activity (U_L higher than –0.50 V) and the ability to suppress HER. C-Ir, N-Os, Fe_2 and $Ru_2@WS_2$ exhibit higher eNRR activity (U_L lower than –0.50 V) and are predicted as the optimal catalysts due to their ability to significantly suppress H_2 generation. It is necessary to further study the proton transfer process over these four catalysts in explicit solvent environments to evaluate the reaction kinetics of eNRR.

3.4 Reaction kinetics

Some previous studies have neglected the kinetics of proton transfer process at the catalyst-electrolyte interface, which may limit the development of predicted catalyst based on reaction thermodynamics in practical applications. The detailed models and computational methods of the simulated kinetics process of proton transfer are shown in Fig. S14 in the ESM. As shown in Fig. 5, the rate-determining step (RDS) for eNRR on N-Os, C-Ir, Fe_2, and $Ru_2@WS_2$ is the first proton transfer step, with free energy barriers of 0.73, 1.08, 0.45, and 0.37 eV at 298.15 K, respectively. As shown in Fig. 5(e), the proton transfer process is triggered by a water molecule of $H_9O_4^+$ near $*N_2$. The transfer of one H from the peripheral water molecules is accompanied by the departure of one H from the central H_3O^+ species, which then rapidly attaches to the remaining OH group to form a new water molecule. In this process, one H of $H_9O_4^+$ is transferred to the distal N of the nitrogen molecule to form the *NNH intermediate and four surrounding

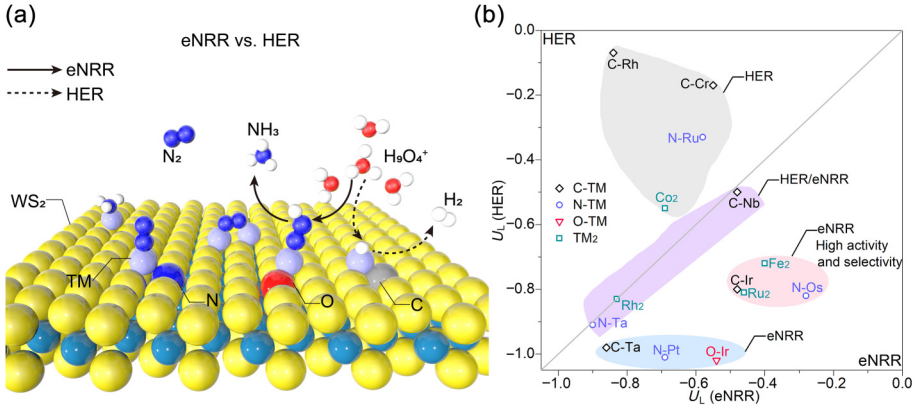

Figure 4 Reaction selectivity. (a) The competitive pathways of eNRR and HER at the active site. (b) Selectivity trend map of eNRR and HER. The catalysts were classified by marking the eNRR activity and selectivity regions with four colors. Red, blue, purple, and gray areas indicate regions with high eNRR activity and selectivity, eNRR activity, HER/eNRR activity, and HER activity, respectively. Color labels: S (yellow), W (dark cyan), N (blue), C (black), O (red), H (white), and active site (lavender).

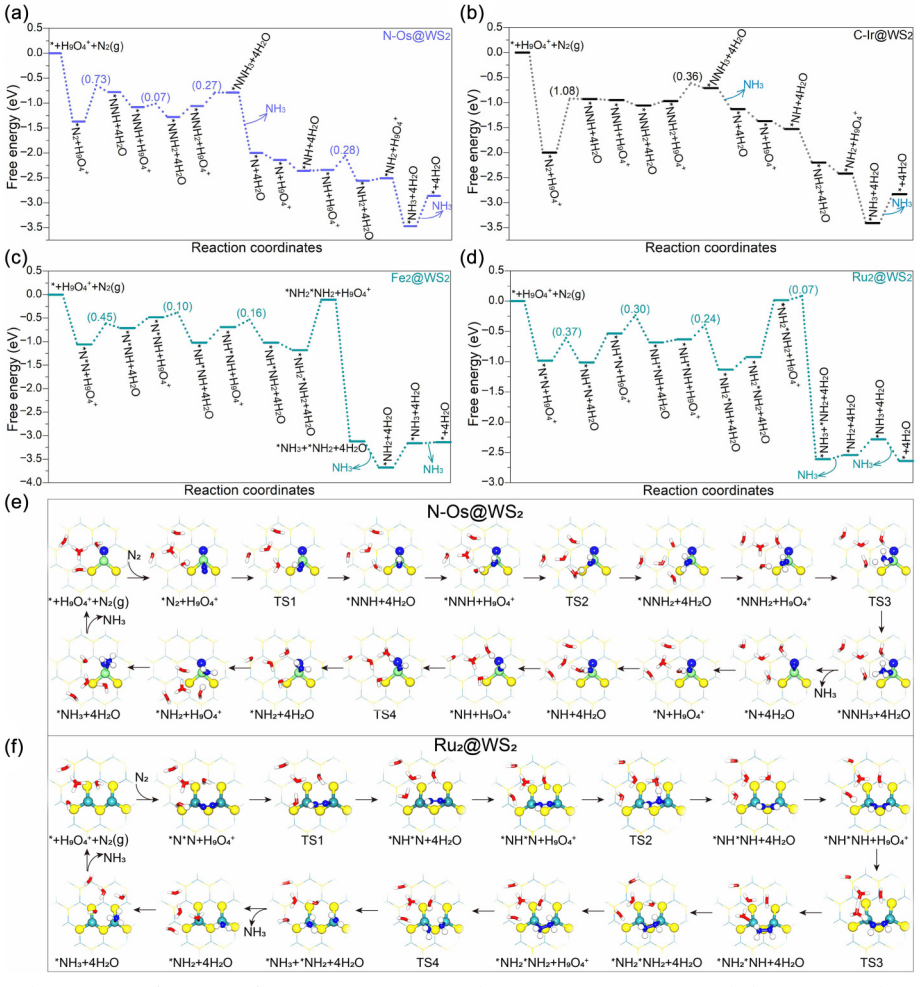

Figure 5 Reaction kinetics. The proton transfer process of eNRR on (a) N-Os@WS_2, (b) C-Ir@WS_2, (c) Fe_2@WS_2, and (d) Ru_2@WS_2 under explicit solvation model. The numbers in parentheses represent the free energy barrier and the temperature is set at 298.15 K. The atomic structures of the initial (IS), transition (TS), and final states (FS) are shown in (e) and (f). The line model represents the WS_2 substrate. Color labels: S (yellow), N (blue), H (white), O (red), Os (green), and Ru (cyan).

water molecules. Subsequently, *NNH is gradually protonated on N-Os@WS_2 SAC through the distal pathway with lower free energy barriers (0.07 to 0.28 eV). In detail, the protonation of *NNH to *NNH_2 is an exothermic process with a free energy barrier of only 0.07 eV. The reduction of *NNH_2 to *NNH_3 requires crossing the free energy barrier of 0.27 eV, where the structure of transition state (TS) is similar to that of final state (FS) in Fig. 5(e). The free energy barrier for hydrogenation of *NH to *NH_2 is 0.28 eV, and the reaction step is thermodynamically exothermic. Some of the proton transfer processes are spontaneous and non-barrier reactions, which are similar to the results of the kinetics of ORR [55]. As shown in Fig. 5(b) and Figs. S14(b)–S14(g) in the ESM, at the

solid–liquid interface of C-Ir@WS_2 SAC, hydrogen bonding exists between H_3O^+ and the surrounding three water molecules, forming an $H_9O_4^+$ species located near $*N_2$. When one H of $H_9O_4^+$ is transferred to $*N_2$, the remaining four water molecules move significantly. *Ab initio* molecular dynamics (AIMD) simulation well reflects the hydrogen bond network and dynamic feature of aqueous solution at solid–liquid interface [56]. As shown in Fig. S14(e) in the ESM, it can be observed from the atomic structure that *NNH in the TS and FS are similar, except that the surrounding water molecules relax. Although the first protonation process on C-Ir@WS_2 SAC is endothermic, the subsequent protonation reaction exhibits a lower free energy barrier (0.36 eV) or barrierless (spontaneity), making the entire eNRR feasible at room temperature. As shown in Figs. 5(c), 5(d), and 5(f), and Fig. S15 in the ESM, the side-on configuration of $*N_2$ on Fe_2 and Ru_2@WS_2 exhibits lower free energy barriers during the protonation process than those in the end-on configuration. For Fe_2@WS_2, the free energy barrier (0.45 eV) of the first protonation of N_2 is lower than that of N-Os@WS_2 (0.73 eV) and C-Ir@WS_2 (1.08 eV), showing more favorable reaction kinetics. The protonation process from *N*NH to *NH*NH is exothermic with a free energy barrier of 0.10 eV. The hydrogenation of *NH*NH to $*NH*NH_2$ is less exothermic with 0.16 eV of free energy barrier, which is 0.06 eV higher than the reaction free energy barrier of the previous step. Other electrochemical steps exhibit spontaneous processes without free energy barriers. Among these four catalysts, only the first protonation reaction of N_2 at Ru_2@WS_2 is exothermic with the lowest free energy barrier (0.37 eV). For Ru_2@WS_2, the free energy barrier of RDS is only about half that of N-Os@WS_2, which indicates that N_2 has a superior adsorption configuration at Ru_2@WS_2, resulting in more back-donation of electrons to the antibonding orbital of N_2 and full activation of the N≡N bond. The free energy barriers for the protonation of *NH*N, *NH*NH, and $*NH_2*NH_2$ on Ru_2@WS_2 are 0.30, 0.24, and 0.07 eV, and these reaction steps are exothermic, which suggests that the electrochemical steps are thermodynamically favorable and less hindered kinetically. Compared with our previous work [26], N-Os@WS_2 and C-Ir@WS_2 have fewer kinetic reaction steps or lower free energy barriers than Os@WS_2 and Ir@WS_2. For example, the free energy barrier of PDS for C-Ir@WS_2 (1.08 eV) is lower than that of Ir@WS_2 (1.15 eV), and the kinetic reaction steps are fewer, thus showing a faster kinetic reaction process, which may be related to the d-orbital occupation of the Ir active site in C-Ir@WS_2. The mechanism of activity enhancement will be discussed in detail in the electronic origin section.

The detailed method of microkinetic modeling is shown in the ESM. Figure 6 shows the turn-over frequency (TOF) of eNRR at different temperatures (300 to 1000 K) and pressures (0 to 100 bar). TOF increases rapidly with the increase of temperature and pressure. Increasing the pressure can improve the adsorption of N_2, and high temperature can reduce the kinetic energy barrier of protonation step. When the temperature is 400 K, the TOF of N-Os, C-Ir, Fe_2 and Ru_2@WS_2 are 80.81, 3.17×10^{-3}, 2.71×10^{5} and 2.75×10^{6} s^{-1}·$site^{-1}$, respectively. Microkinetic modeling (MKM) analysis suggests that Fe_2 and Ru_2@WS_2 have more advantages in reaction kinetics than N-Os and C-Ir@WS_2 SACs. At 400 K, the TOF of Ru_2@WS_2 is higher than that of the reported 2P@C_2N (8.9×10^{5} s^{-1}·$site^{-1}$) [57].

3.5 Electronic origin

Analysis of the electronic structure of catalysts is an effective way to understand the activity of eNRR. Figure 7(a) illustrates that

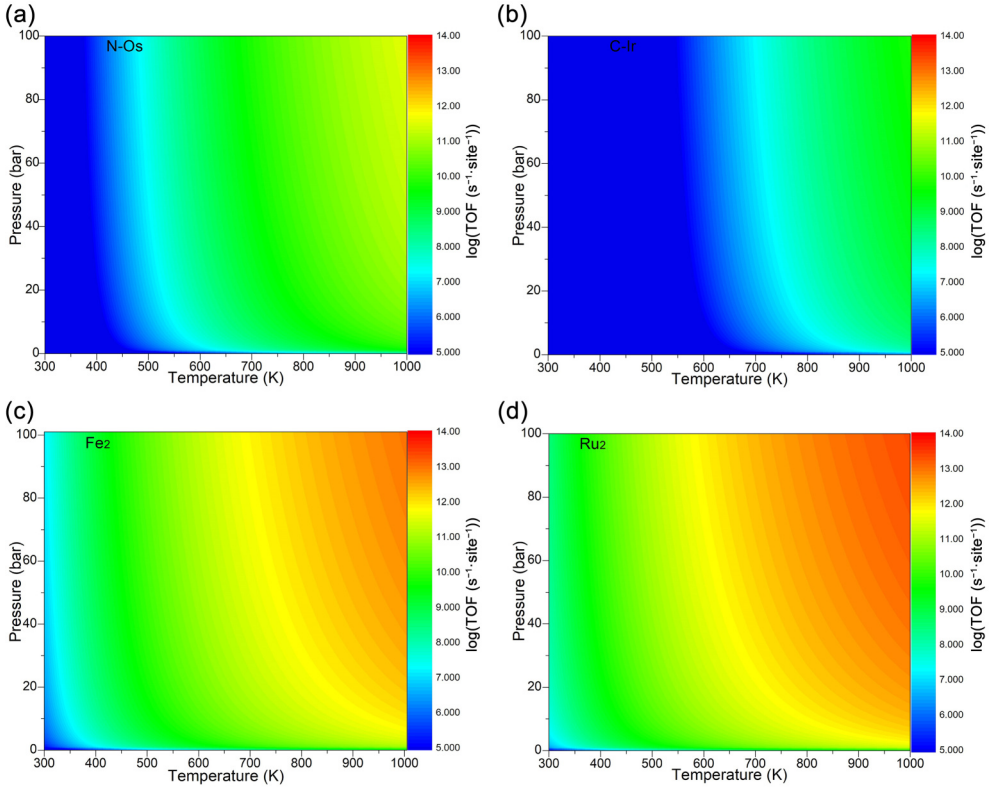

Figure 6 Steady state of microkinetic modeling. The TOF of eNRR as a function of temperature and pressure on (a) N-Os@WS_2, (b) C-Ir@WS_2, (c) Fe_2@WS_2, and (d) Ru_2@WS_2.

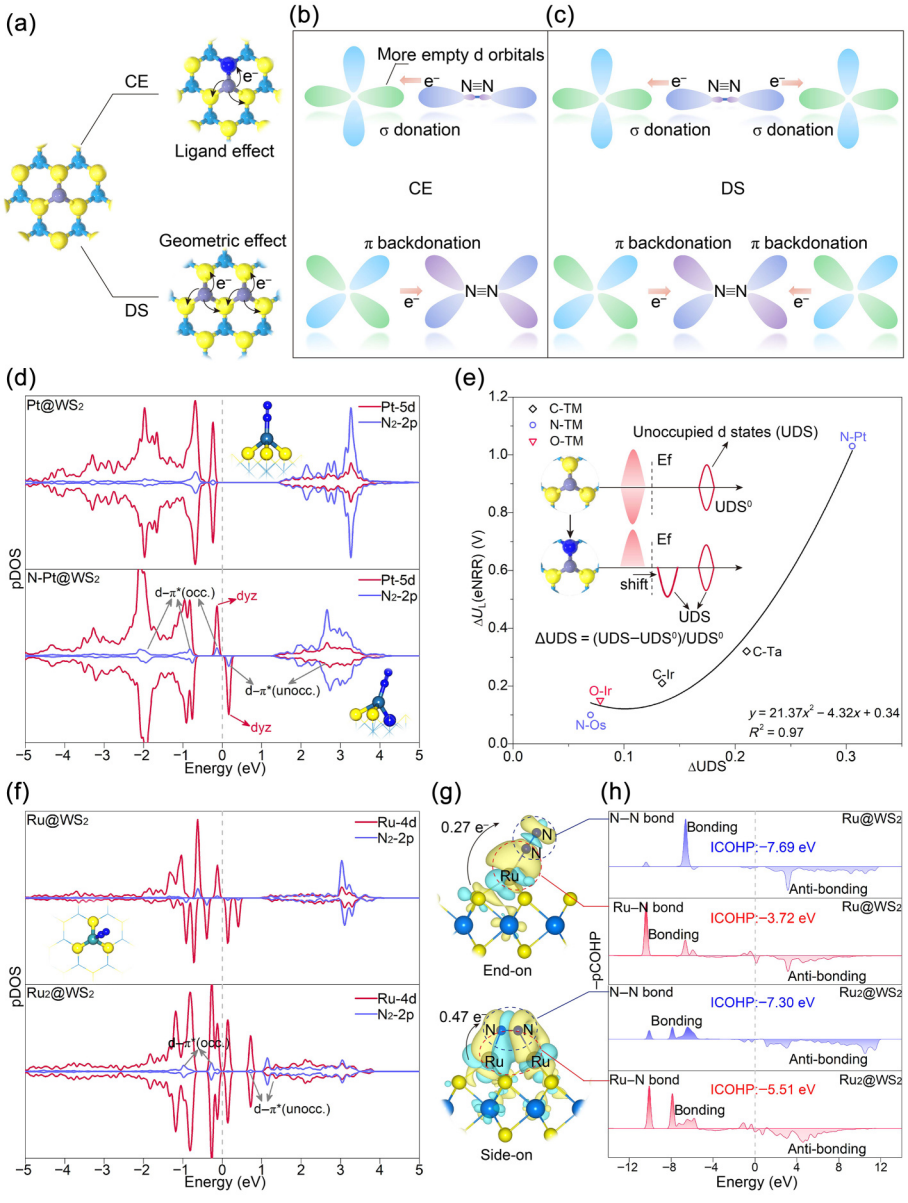

Figure 7 Electronic interpretation of enhanced eNRR activity. (a) Schematic diagram of modulating TM@WS_2 SACs by CE and DS strategies. (b) Schematic diagram of N_2 adsorption on TM: (b) SAC and (c) DS. (d) Projected density of states (pDOS) of N_2 adsorbed on Pt@WS_2 and N-Pt@WS_2 SACs. (e) The relationship between ΔUDS and ΔU_L. The definition of ΔUDS is shown in this figure, ΔU_L equals the difference between the U_L of the modulated TM@WS_2 (C-TM@WS_2, N-TM@WS_2, and O-TM@WS_2) and the TM@WS_2 SACs. (f) pDOS, (g) CDD, and (h) COHP of N_2 adsorption on Ru@WS_2 and Ru_2@WS_2. The Fermi level is set to 0. The yellow and blue regions represent electrons accumulation and depletion. The isosurface is set to 0.001 e·Å^{-3}.

compared to TM@WS_2 SACs, CE and DS strategies (C, N, O-TM@WS_2 SACs and TM_2@WS_2) modulate the electron transfer between the support and active sites, further modulating the eNRR activity through ligand (coordination environment of TM SA) and geometric effects (side-on adsorption configuration of N_2 on TM DS). Figure 7(b) shows that modulating the coordination environment of TM active site leads to a greater electron loss of TM, resulting in the increase of unoccupied d states (UDS) of TM atom. More UDS of TM is advantageous for the σ-donation of N_2 adsorption, followed by the electron transfer from occupied d orbitals to the antibonding π* orbitals of N_2, enabling the effective adsorption and activation of N_2. Figure 7(c) shows a schematic diagram of electron transfer during the adsorption and activation of N_2 by TM DS. Compared to TM@WS_2 SAC, TM_2@WS_2 provides an additional adsorption site for N_2, which leads to a preference for N_2 adsorption on TM_2@WS_2 in the side-on configuration. The electron donation-backdonation process occurs through a dual-channel (two TM-N bonds) between TM DS and N_2, which leads to a significant activation of the N≡N bond.

As shown in Fig. 7(d), for N_2 adsorption on Pt@WS_2 SAC, the highest occupied state is mainly contributed by the Pt-d_{yz} state. For the N-doped Pt@WS_2 SAC, the spin-down d_{yz} moves above the Fermi level to form UDS, which will significantly enhance the d-π* interaction, and the activity of N-Pt@WS_2 SAC is much higher than that of Pt@WS_2 SAC. We selected the SACs with eNRR activity in Fig. 4(b) and calculated the UDS of TM. The inset in Fig. 7(e) suggests that the partially occupied d orbital of TM@WS_2 SAC moves to the unoccupied state after modulating the coordination environment of TM, resulting in a significant difference in UDS between TM@WS_2 SAC and modulated TM@WS_2 SAC. The

change rate (ΔUDS) of the modulated UDS relative to the primitive UDS^0 is correlated with the change amount of activity enhancement (ΔU_L), and it is found that the more change rate of UDS increases, the higher the eNRR activity increases.

The electronic metal-support interaction (EMSI) modulates the d-band center and oxidation state of Pt single atoms on WS_2, where the weakly positive charge state of Pt weakens the adsorption ability of H under acidic conditions, ultimately leading to high HER activity [29]. In our work, it was found that the d-electronic states of Pt active site in Pt@WS_2 SAC can be modulated by N-doping, leading to a reversal in eNRR and HER activity. Bader charge analysis shows that Pt in Pt@WS_2 SAC loses only 0.03 electrons, while Pt in N-Pt@WS_2 SAC loses more electrons (0.22e). Compared to Pt@WS_2 SAC, the UDS of Pt in the N-Pt@WS_2 SAC is enlarged, triggering the electron transfer process between Pt and N_2, resulting in N-Pt@WS_2 SAC exhibiting higher eNRR activity than Pt@WS_2 SAC. The charge state of Pt in N-Pt@WS2 SAC is more positive than that in Pt@WS_2 SAC, which makes the adsorption of H stronger in N-Pt@WS_2 (–1.01 eV) compared with Pt@WS_2 SAC (–0.07 eV) [26], resulting in the lower HER activity of N-Pt@WS_2 under acidic conditions. Modulating the oxidation state and d-electronic structure of Pt SAC through CE is a potential means to reverse the activity of eNRR and HER, which theoretically provides new ideas for experimental researchers to design catalysts.

The difference of eNRR activity can be explained by comparing the electronic structure of N_2 adsorbed on Ru@WS_2 SAC and Ru_2@WS_2. As shown in Fig. 7(f), the d-p orbital overlap of Ru_2@WS_2 is significantly stronger than that of Ru@WS_2 SAC, indicating that the adsorption strength of N_2 in a side-on configuration on Ru_2@WS_2 is stronger than that in an end-on configuration on Ru@WS_2 SAC. Charge density difference (CDD) analysis shown in Fig. 7(g) indicates that there is electron accumulation in both Ru–N bonds of N_2 adsorbed on the Ru_2@WS_2, revealing a dual-channel electron transfer mechanism. In contrast, the CDD analysis shows that there is electron distribution only in one Ru–N bond of N_2 adsorbed on the Ru@WS_2, indicating a single-channel electron transfer mechanism. Bader charge analysis further reveals that the adsorption of N_2 on the Ru_2@WS_2 leads to a transfer of 0.47 electrons from the active site to N_2, while the adsorption of N_2 on the Ru@WS_2 only results in a transfer of 0.27 electrons. As shown in Fig. 7(h), by comparing the crystal orbital Hamilton population (COHP) and integrated COHP (ICOHP) of the N≡N bond and Ru–N bonds for N_2 adsorbed on the Ru@WS_2 SAC and Ru_2@WS_2, it was found that the bonding state contribution (ICOHP: –7.69 eV) of the N≡N bond in the Ru@WS_2 is larger than –7.30 eV in the Ru_2@WS_2 below the Fermi level. This indicates that the N≡N bond is significantly weakened on the Ru_2@WS_2. In the occupied states, the Ru–N bonds in the Ru_2@WS_2 have a larger bonding state contribution (ICOHP: –5.51 eV) compared to that in the Ru@WS_2 (ICOHP: –3.72 eV), indicating that the adsorption of N_2 is stronger on the Ru_2@WS_2. Compared to SAC, TM DS can alter the adsorption configuration of N_2, triggering more significant electron transfer and activation of the N≡N bond, thereby enhancing the eNRR activity.

3.6 Stability of catalysts in solvent environment

The stability of catalyst in solvent environment will affect its electrocatalytic performance. We constructed interface systems of catalysts and explicit water molecules (including 42 explicit water molecules and one H_3O^+) to simulate the dissolution and diffusion processes of active metal atoms in solvent environment. The constructed catalyst-water interfaces of N-Os@WS_2, C-Ir@WS_2, Fe_2@WS_2, and Ru_2@WS_2 are equilibrated at 300 K for 10 ps with a Nosé-Hoover thermostat (detailed AIMD parameter settings are discussed in Fig. S14 in the ESM). As the simulation time of AIMD increases gradually, the temperature and energy oscillate in a small range, and the geometric structures of catalysts preserve well, indicating that the designed catalysts are thermodynamically stable in the solvent environment at room temperature (Figs. S16–S19 in the ESM). We employed the slow-growth method with a step size of 0.0008 and 0.0005 Å for the dissolution and diffusion processes of active metal atoms at the catalyst–water interface. This method has recently been used to study the dynamic process of Cu single atoms leaching from the carbon support and aggregating to form Cu clusters [58]. At 300 K, we found that the free energy barriers for the dissolution (metal atoms migrate from the surface of the WS_2 support to the aqueous solvent) and diffusion processes (metal atoms diffuse on the surface of the WS_2 support from the original position to another anchoring site) of Os, Ir, Fe, and Ru atoms in aqueous solvent environment were greater than 2 eV (Figs. 8 and 9), which suggests that the designed catalysts have a certain level of resistance to leaching and aggregation under solvent conditions.

Compared with the current experimentally synthesized Ru-N-C SAC (theoretical U_L: –0.73 and –0.77 V) and FeCo DAC (theoretical U_L: –0.767 V) with high eNRR performance [59, 60], the designed N-Os@WS_2 and Fe_2@WS_2 have lower theoretical U_L (–0.28 and –0.40 V) in this work. In addition, the stability of TM atoms on WS_2 support in solvent environment also ensures metal loading to a certain extent, so we can reasonably guess that the designed catalysts in our work may exhibit higher ammonia yield rate under practical conditions. However, it is extremely challenging to ensure the stability of the catalyst at high current density, which will stimulate us to further explore the deactivation mechanism of the catalyst under actual voltage in future work. Although we do not discuss the detailed mechanism and catalytic activity of the designed catalysts in electrocatalytic hydrogen oxidation reaction (HOR) or ORR, we anticipate that there may be partial catalysts suitable for fuel cells. For example, in Fig. 4(b), C-Rh@WS_2 has an H adsorption free energy of 0.07 eV, which preliminarily indicates that the H binding capacity of C-Rh@WS_2 may be conducive to HOR because an optimal HOR catalyst should have ΔG(*H) close to zero according to the Sabatier principle [61], but the complete reaction free energy potential energy surface needs to be strictly constructed by subsequent work. Under complex electrochemical conditions, it is very difficult to identify the true structure of the active site and reaction intermediates, which requires AIMD combined with *in-situ* experimental techniques to explore the elusive electrocatalytic mechanism [62–64].

4 Conclusions

In this study, we proposed CE and DS strategies to surpass the Sabatier's limitation of eNRR activity. The LSR between ΔG(*N_2→*N_2H) and ΔG(*NH_2→*NH_3) of TM@WS_2 SACs can be optimized by CE and DS strategies, bringing the modulated catalyst closer to the ideal active space of eNRR. It was found that N-doped WS_2 supported Os SAC (N-Os@WS_2) possessed the highest eNRR activity, which exceeded the best catalyst among TM@WS_2 SACs. Combined with the eNRR selectivity descriptor, we obtained four catalysts with high activity and selectivity, i.e., N-Os, C-Ir, Fe_2 and Ru_2@WS_2. The proton transfer kinetics and multi-scale

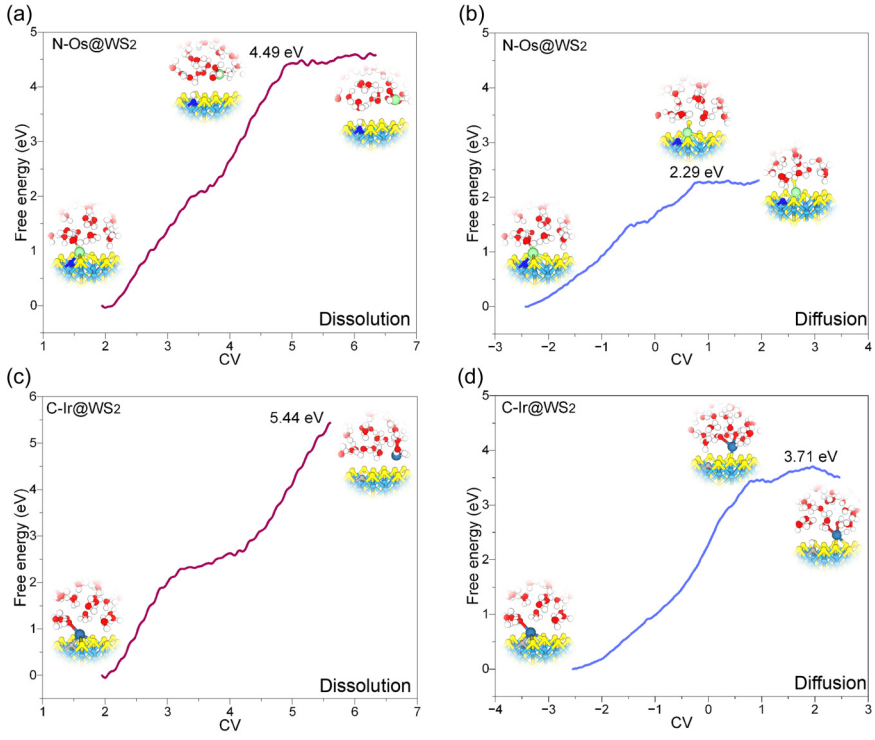

Figure 8 Dynamic processes of dissolution and diffusion of Os and Ir atoms. Free energy profiles for (a) dissolution and (b) diffusion of Os atoms on N-doped WS_2. Free energy profiles for (c) dissolution and (d) diffusion of Ir atoms on C-doped WS_2. The collective variables (CV) for dissolution and diffusion of metal atoms are defined as the distance between the metal atoms and their ligand atoms (C, N, and S atoms). Color labels: S (yellow), W (cyan), N (blue), H (white), O (red), Os (green), and Ir (dark cyan).

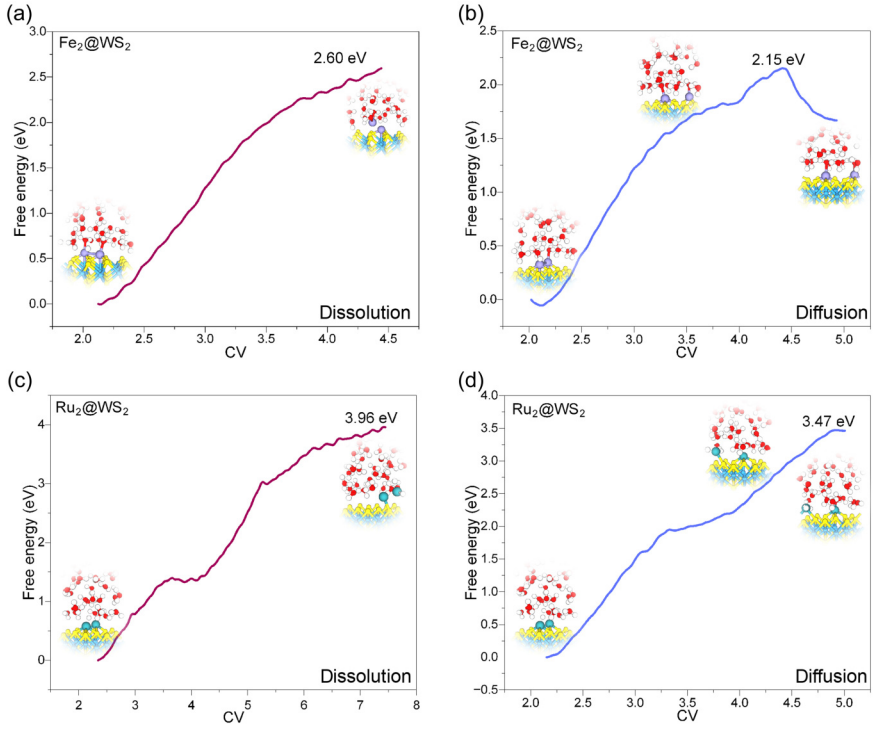

Figure 9 Dynamic processes of dissolution and diffusion of Fe and Ru atoms. Free energy profiles for (a) dissolution and (b) diffusion of Fe atoms on WS_2. Free energy profiles for (c) dissolution and (d) diffusion of Ru atoms on WS_2. The CV for dissolution and diffusion of metal atoms are defined as the distance between the metal atoms and their ligand atoms (S atoms). Color labels: S (yellow), W (cyan), H (white), O (red), Fe (lavender), and Ru (ultramarine).

microkinetic modeling were conducted by using explicit solvation model over the screened catalysts. The electronic structure analysis showed that CE and DS strategies could enhance the donation-backdonation of electron transfer between N_2 and active sites through ligand effect and geometric effect, respectively, thereby improving the eNRR activity. The designed catalysts showed certain

stability in the simulated solvent environment. This work not only elucidates the structure–activity relationship of SACs at the electronic level and provides feasible catalytic design strategies to enhance the eNRR performance of SACs, but also holds reference value for other electrochemical reactions involving multiple proton-electron transfers.

Electronic Supplementary Material: Supplementary Material (computational details for calculating the free energy, binding energy, dissolution potential, adsorption energy, free energy barrier and microkinetic modeling; geometrical structures of catalysts, intermediates and explicit models; free energy diagrams of eNRR on screened catalysts; AIMD simulations) is available in the online version of this article at https://doi.org/10.26599/NR.2025.94907212.

Data availability

All data needed to support the conclusions in the paper are presented in the manuscript and the Electronic Supplementary Material. Additional data related to this paper may be requested from the corresponding author upon request.

Acknowledgments

This work was financially supported by the National Natural Science Foundation of China (No. 51971037). We gratefully acknowledge HZWTECH for providing computation facilities.

Declaration of competing interest

All the contributing authors report no conflict of interests in this work.

Author contribution statement

R. Y. L.: Data curation, validation, writing manuscript, experimental design. C. M. W.: Data curation, validation. J. Z.: Data curation. W. G.: Project administration, funding acquisition. All the authors have approved the final manuscript.

Use of AI statement

None.

References

[1] Liu, X.; Jiao, Y.; Zheng, Y.; Jaroniec, M.; Qiao, S. Z. Building up a picture of the electrocatalytic nitrogen reduction activity of transition metal single-atom catalysts. *J. Am. Chem. Soc.* **2019**, *141*, 9664–9672.

[2] Wan, Y. J.; Chen, W. B.; Wu, S. Q.; Gao, S.; Xiong, F.; Guo, W. H.; Feng, L.; Cai, K. T.; Zheng, L. R.; Wang, Y. G. et al. Confinement engineering of zinc single-atom triggered charge redistribution on Ruthenium site for alkaline hydrogen production. *Adv. Mater.* **2024**, *36*, 2308798.

[3] Hai, X.; Zheng, Y.; Yu, Q.; Guo, N.; Xi, S. B.; Zhao, X. X.; Mitchell, S.; Luo, X. H.; Tulus, V.; Wang, M. et al. Geminal-atom catalysis for cross-coupling. *Nature* **2023**, *622*, 754–760.

[4] Su, J. W.; Wan, Y. J.; Feng, L.; Huang, D. D.; Chu, H. K.; Zhang, X.; Geng, X. Y.; Wang, Y. G.; Zhong, R. Q.; Zou, R. Q. "One-stone, two-birds": Zinc-rich metal-organic frameworks as precursors for high-entropy Zn-air battery electrocatalysts with hierarchical pore structures. *Angew. Chem., Int. Ed.*, in press, https://doi.org/10.1002/anie.202413826.

[5] Chen, J. F.; Jia, M. L.; Wang, J. L.; Hu, P. J.; Wang, H. F. Breaking through the peak height limit of the volcano-shaped activity curve for metal catalysts: Role of distinct surface structures on transition metal oxides. *J. Phys. Chem. C* **2022**, *126*, 183–191.

[6] Nwaokorie, C. F.; Montemore, M. M. Alloy catalyst design beyond the volcano plot by breaking scaling relations. *J. Phys. Chem. C* **2022**, *126*, 3993–3999.

[7] Li, R. Y.; Wang, C. M.; Liu, Y. Z.; Suo, C. X.; Zhang, D. Y.; Zhang, J.; Guo, W. Computational screening of defective BC_3-supported single-atom catalysts for electrochemical CO_2 reduction. *Phys. Chem. Chem. Phys.* **2024**, *26*, 18285–18301.

[8] Abild-Pedersen, F.; Greeley, J.; Studt, F.; Rossmeisl, J.; Munter, T. R.; Moses, P. G.; Skúlason, E.; Bligaard, T.; NØrskov, J. K. Scaling properties of adsorption energies for hydrogen-containing molecules on transition-metal surfaces. *Phys. Rev. Lett.* **2007**, *99*, 016105.

[9] Ding, J.; Li, F. H.; Zhang, J. C.; Zhang, Q.; Liu, Y. H.; Wang, W. J.; Liu, W.; Wang, B. B.; Cai, J.; Su, X. Z. et al. Circumventing CO_2 reduction scaling relations over the heteronuclear diatomic catalytic pair. *J. Am. Chem. Soc.* **2023**, *145*, 11829–11836.

[10] Liu, F.; Gao, R. J.; Shi, C. X.; Pan, L.; Huang, Z. F.; Zhang, X. W.; Zou, J. J. Avoiding Sabatier's limitation on spatially correlated Pt–Mn atomic pair sites for oxygen electroreduction. *J. Am. Chem. Soc.* **2023**, *145*, 25252–25263.

[11] Skúlason, E.; Bligaard, T.; Gudmundsdóttir, S.; Studt, F.; Rossmeisl, J.; Abild-Pedersen, F.; Vegge, T.; Jónsson, H.; Nørskov, J. K. A theoretical evaluation of possible transition metal electro-catalysts for N_2 reduction. *Phys. Chem. Chem. Phys.* **2012**, *14*, 1235–1245.

[12] Zhao, J. X.; Chen, Z. F. Single Mo atom supported on defective boron nitride monolayer as an efficient electrocatalyst for nitrogen fixation: A computational study. *J. Am. Chem. Soc.* **2017**, *139*, 12480–12487.

[13] Li, W. J.; Lou, Z. X.; Yuan, H. Y.; Yang, H. G.; Wang, H. F. Oriented design of triple atom catalysts for electrocatalytic nitrogen reduction with the genetic-algorithm-based global optimization method driven by first principles calculations. *J. Mater. Chem. A* **2022**, *10*, 16106–16114.

[14] Ye, K.; Hu, M.; Li, Q. K.; Han, Y. L.; Luo, Y.; Jiang, J.; Zhang, G. Z. Cooperative nitrogen activation and ammonia synthesis on densely monodispersed Mo-N-C sites. *J. Phys. Chem. Lett.* **2020**, *11*, 3962–3968.

[15] Ye, K.; Hu, M.; Li, Q. K.; Luo, Y.; Jiang, J.; Zhang, G. Z. Cooperative single-atom active centers for attenuating the linear scaling effect in the nitrogen reduction reaction. *J. Phys. Chem. Lett.* **2021**, *12*, 5233–5240.

[16] Li, R. Y.; Feng, Z.; Li, Y.; Dai, X. Q.; Ma, Y. Q.; Tang, Y. N. Bioinspired Mo tape-porphyrin as an efficient and selective electrocatalyst for ammonia synthesis. *Appl. Surf. Sci.* **2020**, *520*, 146202.

[17] Xu, Y. K.; Cai, Z. W.; Du, P.; Zhou, J. X.; Pan, Y. H.; Wu, P.; Cai, C. X. Taming the challenges of activity and selectivity in the electrochemical nitrogen reduction reaction using graphdiyne-supported double-atom catalysts. *J. Mater. Chem. A* **2021**, *9*, 8489–8500.

[18] Long, J.; Fu, X. Y.; Xiao, J. P. The rational design of single-atom catalysts for electrochemical ammonia synthesis via a descriptor-based approach. *J. Mater. Chem. A* **2020**, *8*, 17078–17088.

[19] Zheng, M.; Xu, H. B.; Li, Y.; Ding, K. N.; Zhang, Y. F.; Sun, C. H.; Chen, W. K.; Lin, W. Electrocatalytic nitrogen reduction by transition metal single-atom catalysts on polymeric carbon nitride. *J. Phys. Chem. C.* **2021**, *125*, 13880–13888.

[20] Xiao, Y.; Shen, C.; Long, T. Theoretical establishment and screening of an efficient catalyst for N_2 electroreduction on two-dimensional transition-metal borides (MBenes). *Chem. Mater.* **2021**, *33*, 4023–4034.

[21] Lin, X. Y.; Li, L. L.; Chang, X.; Pei, C. L.; Zhao, Z. J.; Gong, J. L. Black phosphorus-hosted single-atom catalyst for electrocatalytic nitrogen reduction. *Sci. China Mater.* **2021**, *64*, 1173–1181.

[22] Qin, Y. Y.; Li, Y.; Zhao, W. S.; Chen, S. H.; Wu, T. T.; Su, Y. Q. Computational study of transition metal single-atom catalysts supported on nitrogenated carbon nanotubes for electrocatalytic nitrogen reduction. *Nano Res.* **2023**, *16*, 325–333.

[23] Ji, Y. F.; Liu, P. Y.; Huang, Y. G. First-principles screening of transition metal doped anatase TiO_2(101) surfaces for the electrocatalytic nitrogen reduction. *Phys. Chem. Chem. Phys.* **2023**, *25*, 5827–5835.

[24] Zhai, X. W.; Li, L.; Liu, X. Y.; Li, Y. F.; Yang, J. M.; Yang, D. Z.; Zhang, J. L.; Yan, H. X.; Ge, G. X. A DFT screening of single transition atoms supported on MoS_2 as highly efficient electrocatalysts for the nitrogen reduction reaction. *Nanoscale* **2020**, *12*, 10035–10043.

[25] Cai, L. J.; Zhang, N.; Qiu, B. C.; Chai, Y. Computational design of transition metal single-atom electrocatalysts on PtS_2 for efficient nitrogen reduction. *ACS Appl. Mater. Interfaces* **2020**, *12*, 20448–20455.

[26] Li, R. Y.; Guo, W. Screening of transition metal single-atom catalysts supported by a WS_2 monolayer for electrocatalytic nitrogen reduction reaction: Insights from activity trend and descriptor. *Phys. Chem. Chem. Phys.* **2022**, *24*, 13384–13398.

[27] Li, L. B.; Yuan, K.; Chen, Y. W. Breaking the scaling relationship limit: From single-atom to dual-atom catalysts. *Acc. Mater. Res.* **2022**, *3*, 584–596.

[28] Ouyang, Y. X.; Shi, L.; Bai, X. W.; Li, Q.; Wang, J. L. Breaking scaling relations for efficient CO_2 electrochemical reduction through dual-atom catalysts. *Chem. Sci.* **2020**, *11*, 1807–1813.

[29] Shi, Y.; Ma, Z. R.; Xiao, Y. Y.; Yin, Y. C.; Huang, W. M.; Huang, Z. C.; Zheng, Y. Z.; Mu, F. Y.; Huang, R.; Shi, G. Y. et al. Electronic metal-support interaction modulates single-atom platinum catalysis for hydrogen evolution reaction. *Nat. Commun.* **2021**, *12*, 3021.

[30] Mariappan, A.; Dharman, R. K.; Oh, T. H. Efficient visible light photocatalytic degradation of heavy metal pollutant using carbon doped WS_2 nanostructure. *Opt. Mater.* **2023**, *135*, 113366.

[31] Sun, C. Q.; Zhang, J. Y.; Ma, J.; Liu, P. T.; Gao, D. Q.; Tao, K.; Xue, D. S. N-doped WS_2 nanosheets: A high-performance electrocatalyst for the hydrogen evolution reaction. *J. Mater. Chem. A* **2016**, *4*, 11234–11238.

[32] Cui, Q. L.; Luo, Z. Y.; Cui, Q. R.; Zhu, W.; Shou, H. W.; Wu, C. Q.; Liu, Z. F.; Lin, Y. X.; Zhang, P. J.; Wei, S. Q. et al. Robust and high photoluminescence in WS_2 monolayer through *in situ* defect engineering. *Adv. Funct. Mater.* **2021**, *31*, 2105339.

[33] Fu, J. H.; Dong, J. H.; Si, R.; Sun, K. J.; Zhang, J. Y.; Li, M. R.; Yu, N. N.; Zhang, B. S.; Humphrey, M. G.; Fu, Q. et al. Synergistic effects for enhanced catalysis in a dual single-atom catalyst. *ACS Catal.* **2021**, *11*, 1952–1961.

[34] Lou, Y.; Jiang, F.; Zhu, W.; Wang, L.; Yao, T. Y.; Wang, S. S.; Yang, B.; Yang, B.; Zhu, Y. F.; Liu, X. H. CeO_2 supported Pd dimers boosting CO_2 hydrogenation to ethanol. *Appl. Catal. B: Environ.* **2021**, *291*, 120122.

[35] Zhu, J. B.; Xiao, M. L.; Ren, D. Z.; Gao, R.; Liu, X. Z.; Zhang, Z.; Luo, D.; Xing, W.; Su, D.; Yu, A. P. et al. Quasi-covalently coupled Ni–Cu atomic pair for synergistic electroreduction of CO_2. *J. Am. Chem. Soc.* **2022**, *144*, 9661–9671.

[36] Wang, X. K.; Xu, L. L.; Li, C.; Zhang, C. H.; Yao, H. X.; Xu, R.; Cui, P. X.; Zheng, X. S.; Gu, M.; Lee, J. et al. Developing a class of dual atom materials for multifunctional catalytic reactions. *Nat. Commun.* **2023**, *14*, 7210.

[37] Chai, Y. C.; Chen, S. H.; Chen, Y.; Wei, F. F.; Cao, L. R.; Lin, J.; Li, L.; Liu, X. Y.; Lin, S.; Wang, X. D. et al. Dual-atom catalyst with N-colligated Zn_1Co_1 species as dominant active sites for propane dehydrogenation. *J. Am. Chem. Soc.* **2024**, *146*, 263–273.

[38] Zheng, J. W.; Lebedev, K.; Wu, S.; Huang, C.; Ayvalı, T.; Wu, T. S.; Li, Y. Y.; Ho, P. L.; Soo, Y. L.; Kirkland, A. et al. High loading of transition metal single atoms on chalcogenide catalysts. *J. Am. Chem. Soc.* **2021**, *143*, 7979–7990.

[39] Kresse, G.; Furthmüller, J. Efficient iterative schemes for *ab initio* total-energy calculations using a plane-wave basis set. *Phys. Rev. B* **1996**, *54*, 11169–11186.

[40] Kresse, G.; Furthmüller, J. Efficiency of *ab-initio* total energy calculations for metals and semiconductors using a plane-wave basis set. *Comput. Mater. Sci.* **1996**, *6*, 15–50.

[41] Hongzhiwei Technology, Device Studio, Version 2023A, China, 2025 [Online]. https://cloud.hzwtech.com/web/home.

[42] Blöchl, P. E. Projector augmented-wave method. *Phys. Rev. B* **1994**, *50*, 17953–17979.

[43] Perdew, J. P.; Burke, K.; Ernzerhof, M. Generalized gradient approximation made simple. *Phys. Rev. Lett.* **1996**, *77*, 3865–3868.

[44] Monkhorst, H. J.; Pack, J. D. Special points for Brillouin-zone integrations. *Phys. Rev. B* **1976**, *13*, 5188–5192.

[45] Grimme, S.; Ehrlich, S.; Goerigk, L. Effect of the damping function in dispersion corrected density functional theory. *J. Comput. Chem.* **2011**, *32*, 1456–1465.

[46] Li, M. Y.; Cui, Y.; Sun, L. P.; Zhang, X. L.; Peng, L.; Huang, Y. C. Boosting electrocatalytic N_2 reduction to NH_3 over two-dimensional gallium selenide by defect-size engineering. *Inorg. Chem.* **2020**, *59*, 4858–4867.

[47] Huang, Y.; Yang, T. T.; Yang, L.; Liu, R.; Zhang, G. Z.; Jiang, J.; Luo, Y.; Lian, P.; Tang, S. B. Graphene-boron nitride hybrid-supported single Mo atom electrocatalysts for efficient nitrogen reduction reaction. *J. Mater. Chem. A* **2019**, *7*, 15173–15180.

[48] Johnson, L. R.; Sridhar, S.; Zhang, L.; Fredrickson, K. D.; Raman, A. S.; Jang, J.; Leach, C.; Padmanabhan, A.; Price, C. C.; Frey, N. C. et al. MXene materials for the electrochemical nitrogen reduction-functionalized or not. *ACS Catal.* **2020**, *10*, 253–264.

[49] Mathew, K.; Sundararaman, R.; Letchworth-Weaver, K.; Arias, T. A.; Hennig, R. G. Implicit solvation model for density-functional study of nanocrystal surfaces and reaction pathways. *J. Chem. Phys.* **2014**, *140*, 084106.

[50] Guo, X. Y.; Gu, J. X.; Lin, S. R.; Zhang, S. L.; Chen, Z. F.; Huang, S. P. Tackling the activity and selectivity challenges of electrocatalysts toward the nitrogen reduction reaction via atomically dispersed Biatom catalysts. *J. Am. Chem. Soc.* **2020**, *142*, 5709–5721.

[51] Zhang, L.; Ji, X. Q.; Ren, X.; Ma, Y. J.; Shi, X. F.; Tian, Z. Q.; Asiri, A. M.; Chen, L.; Tang, B.; Sun, X. P. Electrochemical ammonia synthesis via nitrogen reduction reaction on a MoS_2 catalyst: Theoretical and experimental studies. *Adv. Mater.* **2018**, *30*, 1800191.

[52] Wang, S. H.; Wei, W.; Lv, X. S.; Huang, B. B.; Dai, Y. W supported on g-CN manifests high activity and selectivity for N_2 electroreduction to NH_3. *J. Mater. Chem. A* **2020**, *8*, 1378–1385.

[53] Ling, C. Y.; Ouyang, Y. X.; Li, Q.; Bai, X. W.; Mao, X.; Du, A. J.; Wang, J. L. A general two-step strategy-based high-throughput screening of single atom catalysts for nitrogen fixation. *Small Methods* **2019**, *3*, 1800376.

[54] Liang, X. Y.; Deng, X. X.; Guo, C.; Wu, C. M. L. Activity origin and design principles for atomic vanadium anchoring on phosphorene monolayer for nitrogen reduction reaction. *Nano Res.* **2020**, *13*, 2925–2932.

[55] Wang, Y.; Tang, Y. J.; Zhou, K. Self-adjusting activity induced by intrinsic reaction intermediate in Fe-N-C single-atom catalysts. *J. Am. Chem. Soc.* **2019**, *141*, 14115–14119.

[56] Tian, Y. M.; Hou, P. F.; Zhang, H. W.; Xie, Y.; Chen, G.; Li, Q.; Du,

F.; Vojvodic, A.; Wu, J. Z.; Meng, X. Theoretical insights on potential-dependent oxidation behaviors and antioxidant strategies of MXenes. *Nat. Commun.* **2024**, *15*, 10099.

[57] Wu, Q.; Wang, H.; Shen, S. Y.; Huang, B. B.; Dai, Y.; Ma, Y. D. Efficient nitric oxide reduction to ammonia on a metal-free electrocatalyst. *J. Mater. Chem. A* **2021**, *9*, 5434–5441.

[58] Zhang, J.; Wang, Y.; Li, Y. F. Not one, not two, but at least three: Activity origin of copper single-atom catalysts toward CO_2/CO electroreduction to C_{2+} products. *J. Am. Chem. Soc.* **2024**, *146*, 14954–14958.

[59] Geng, Z. G.; Liu, Y.; Kong, X. D.; Li, P.; Li, K.; Liu, Z. Y.; Du, J. J.; Shu, M.; Si, R.; Zeng, J. Achieving a record-high yield rate of 120.9 $\mu g_{NH_3} \cdot mg_{cat.}^{-1} \cdot h^{-1}$ for N_2 electrochemical reduction over Ru single-atom catalysts. *Adv. Mater.* **2018**, *30*, 1803498.

[60] Zhang, S. B.; Han, M. M.; Shi, T. F.; Zhang, H. M.; Lin, Y.; Zheng, X. S.; Zheng, L. R.; Zhou, H. J.; Chen, C.; Zhang, Y. X. et al. Atomically dispersed bimetallic Fe-Co electrocatalysts for green production of ammonia. *Nat. Sustain.* **2023**, *6*, 169–179.

[61] Wang, X. N.; Tong, Y. F.; Feng, W. T.; Liu, P. Y.; Li, X. J.; Cui, Y. P.; Cai, T. H.; Zhao, L. M.; Xue, Q. Z.; Yan, Z. F. et al. Embedding oxophilic rare-earth single atom in platinum nanoclusters for efficient hydrogen electro-oxidation. *Nat. Commun.* **2023**, *14*, 3767.

[62] Li, C. Y.; Le, J. B.; Wang, Y. H.; Chen, S.; Yang, Z. L.; Li, J. F.; Cheng, J.; Tian, Z. Q. *In situ* probing electrified interfacial water structures at atomically flat surfaces. *Nat. Mater.* **2019**, *18*, 697–701.

[63] Li, P.; Jiang, Y. L.; Hu, Y. C.; Men, Y.; Liu, Y. W.; Cai, W. B.; Chen, S. L. Hydrogen bond network connectivity in the electric double layer dominates the kinetic pH effect in hydrogen electrocatalysis on Pt. *Nat. Catal.* **2022**, *5*, 900–911.

[64] Li, P.; Jiao, Y. Z.; Ruan, Y. E.; Fei, H. G.; Men, Y.; Guo, C. L.; Wu, Y. E.; Chen, S. L. Revealing the role of double-layer microenvironments in pH-dependent oxygen reduction activity over metal-nitrogen-carbon catalysts. *Nat. Commun.* **2023**, *14*, 6936.